D0 Note 6345-CONF

Updated search for the Standard Model Higgs Boson in the $\gamma\gamma + X$ final state at D0

The D0 Collaboration
URL http://www-d0.fnal.gov
(Dated: June 29, 2012)

This note describes the updated search for a light standard model (SM) Higgs boson (H) in the inclusive diphoton final state based on data corresponding to 9.7 fb^{-1} of $p\bar{p}$ collisions at $\sqrt{s} = 1.96$ TeV collected with the D0 detector at the Fermilab Tevatron Collider. No data excess above the background prediction is observed. We set 95% C.L. upper limits on the ratio of the cross section times the branching ratio ($\sigma \times BR(H \to \gamma\gamma)$) to the SM Higgs boson prediction for different assumed Higgs masses from 100 to 150 GeV. The expected limits are below 10 between 110 and 130 GeV, with a minimum of 8.2 at 125 GeV. The observed limits at 110, 125 and 130 GeV are 8.0, 12.9 and 13.7, respectively.

Preliminary Results for Summer Conferences 2012

I. INTRODUCTION

In the Standard Model (SM), the Higgs boson (H) is the last undiscovered elementary particle and provides crucial insights into the spontaneous breaking of electroweak symmetry and mass generation for the electroweak gauge bosons and fermions. The combination of constraints from direct searches at LEP [1] and from precision electroweak observables [2], including the latest W boson mass measurements from CDF [3] and D0 [4], results in a preferred range for the Higgs boson mass of $114.4 < M_H < 152$ GeV at 95% C.L. The most recent LHC results [5, 6] extend the excluded regions to $112.9 < M_H < 115.5$ and $127 < M_H < 600$ GeV, and show an interesting excess at ~ 125 GeV in the diphoton channel [7, 8] and $H \to ZZ^* \to 4l$ [9, 10]. In this note, we report on a search for the SM Higgs boson in an inclusive event sample containing two photons. The search for this particular decay mode is challenging due to the small di-photon branching ratio of the SM Higgs; the branching ratio reaches its maximum of 0.23% at $M_H = 125$ GeV. On the other hand, the two-photon signature is clean and sensitive to all of the three production mechanisms (gluon-gluon fusion (GF), vector boson associated production (VH), vector boson fusion (VBF)), and leads to an experimental search that can constrain models beyond the SM where this branching ratio can be significantly enhanced [11].

As our previous analysis [12], this search is based on the complete D0 Run II data, corresponding to an integrated luminosity of 9.7 fb^{-1}, and uses a Multivariate Analysis Technique (MVA) [13] to better separate signal and background. The major improvements are calibration of vertexing, photon energy scale and reduction of the impact from systematic uncertainties on the limits, as explained in detail in Section III and V.

II. D0 DETECTOR AND DATA SAMPLE

The D0 detector is comprised of a central tracking system in a 2 T superconducting solenoidal magnet, a liquid-argon/uranium calorimeter, a preshower detector and a muon spectrometer [14]. The major parts of the D0 detector used in the event selection are the tracking system, the electromagnetic (EM) calorimeter and the central preshower detector (CPS). The tracking system consists of a silicon microstrip tracker (SMT) and a scintillating fiber tracker (CFT), providing coverage for charged particles in the pseudorapidity range $|\eta_{det}| \lesssim 3$ [15]. The calorimeter has a central section (CC) covering up to $|\eta_{det}| \approx 1.1$, and two end caps (EC) extending coverage to $|\eta_{det}| \approx 4.2$. Each section is housed in a separate cryostat and divided into EM layers on the inside and hadronic layers on the outside. The EM calorimeter has four longitudinal layers and transverse segmentation of 0.1×0.1 in $\eta_{det} \times \phi_{det}$ [15] space, except in the third layer (EM3) where it is 0.05×0.05. The CPS is positioned immediately before the inner layer of the central EM calorimeter, consisting of 2 radiation lengths of absorber followed by three layers of scintillating strips with embedded wavelength-shifting fibers. Luminosity is measured using plastic scintillator arrays located in front of the EC cryostats. The data acquisition system consists of a three-level trigger, designed to accommodate the high instantaneous luminosity. For final states containing two photon candidates with transverse energy above 25 GeV, the trigger efficiency is close to 100%. The data sample used in this analysis was collected between April 2002 and September 2011 and corresponds to an integrated luminosity of 9.7 ± 0.6 fb^{-1} after applying standard data quality requirements.

The SM Higgs Monte Carlo (MC) samples are generated using PYTHIA [16] with CTEQ6L1 [17] parton distribution functions (PDFs) and processed through a GEANT-3 based [18] simulation of the D0 detector. In order to accurately model the effects of multiple $p\bar{p}$ interactions and detector noise, data events from random $p\bar{p}$ crossings that have an instantaneous luminosity spectrum similar to the events in the analysis are overlaid on the MC events. These MC events are then processed using the same reconstruction software as the data. Samples corresponding to each of the three dominant SM Higgs boson production mechanisms are normalized using the next-to-next-to-leading order (NNLO) theoretical cross sections for gluon fusion and vector boson associated production, and NLO for vector boson fusion production [19]. The branching ratio predictions are from HDECAY [20]. The gluon fusion production cross section is also corrected for two-loop electroweak effects [21].

III. EVENT SELECTION

The $p\bar{p}$ interaction vertex for diphoton events is determined using an algorithm based on the determination of the photons' directions using the calorimeter and preshower information and on the multiplicity of tracks associated to the various interaction vertices reconstructed in a single bunch crossing. When one or both photons reconstructed in the EM calorimeter also deposit part of their energy in the CPS, the algorithm chooses the $p\bar{p}$ interaction vertex whose coordinate along the beam axis is closest to the extrapolation of the photon trajectory determined from the calorimeter and the CPS information, provided the distance between the coordinates of the vertex and of the photon

trajectory is smaller than 3 standard deviations (the uncertainty on this distance is dominated by the uncertainty on the extrapolation of the photon direction). Otherwise the algorithm chooses the $p\bar{p}$ interaction vertex with the largest multiplicity of associated tracks. This algorithm is calibrated and optimized using $Z/\gamma^* \to ee$ data and MC events, that are reconstructed ignoring the track information for the electron pair. This algorithm correctly identifies the $p\bar{p}$ interaction vertex in 95% of the events, an improvement of 20% relative to an algorithm based purely on the multiplicity of associated tracks. In addition, the selected $p\bar{p}$ interaction vertex is required to be within 60 cm of the center of the detector along the beam axis.

In our previous result [12] the energy of the photons was calibrated using the EM energy scale determined from $Z \to ee$ events, which results in an overestimation of the photons' energies, in particular at larger rapidities where an electron loses more energy in the material in front of the calorimeter compared to a photon. For this analysis, we apply a rapidity dependent correction (∼1-5%) based on GEANT simulation of the D0 detector response to compensate for the difference.

Events are selected by requiring at least two photon candidates with $E_T > 25$ GeV and $|\eta_{det}| < 1.1$. Photons are selected from EM clusters reconstructed within a cone of radius $\mathcal{R} = \sqrt{(\Delta\eta)^2 + (\Delta\phi)^2} = 0.2$ and satisfying the following requirements: (i) At least 95% of the cluster energy is deposited in the EM calorimeter. (ii) The calorimeter isolation variable $I = [E_{\rm tot}(0.4) - E_{\rm EM}(0.2)]/E_{\rm EM}(0.2)$ is less than 0.1, where $E_{\rm tot}(0.4)$ is the total energy in a cone of radius $\mathcal{R} = 0.4$ and $E_{\rm EM}(0.2)$ is the EM energy in a cone of radius $\mathcal{R} = 0.2$. (iii) The energy-weighted cluster width in EM3 is consistent with an EM shower. (iv) The scalar sum of the transverse momentum of all tracks originating from the primary vertex in an annulus of $0.05 < \mathcal{R} < 0.4$ around the cluster ($\sum p_T^{\rm trk}$) is less than 2 GeV. (v) In order to suppress electrons misidentified as photons, the EM clusters are required not to be spatially matched to either a reconstructed track or a set of hits in the SMT and CFT consistent with that of an electron trajectory. (vi) The contribution of jets misidentified as photons is reduced by combining the information from a set of variables sensitive to differences between photons and jets in the tracker and in the energy distributions in the calorimeter and CPS, using an artificial neural network (ANN) [22] described below. Photon candidates are required to have an ANN output O_{NN} larger than 0.1. (vii) At least one photon candidate has a match to activity in the CPS. (viii) Additionally, the di-photon invariant mass is required to be larger than 60 GeV.

The ANN used to distinguish photons from jets uses the following variables: $\sum p_T^{\rm trk}$; the number of cells above a certain threshold requirement in the first EM calorimeter layer within $\mathcal{R} < 0.2$ and $0.2 < \mathcal{R} < 0.4$ of the EM cluster; the number of associated CPS clusters within $\mathcal{R} < 0.1$ of the EM cluster; and a measure of the width of the energy deposition in the CPS. The ANN is trained using di-photon and di-jet MC samples and its performance is verified using a data sample of $Z \to \ell^+\ell^-\gamma$ ($\ell = e, \mu$) events [23]. Figure 1 compares the ANN output (O_{NN}) distribution for photons and jets. The photon identification requirement $O_{NN} > 0.1$ is almost 100% efficient for photons while rejecting ∼ 40% of misidentified jets.

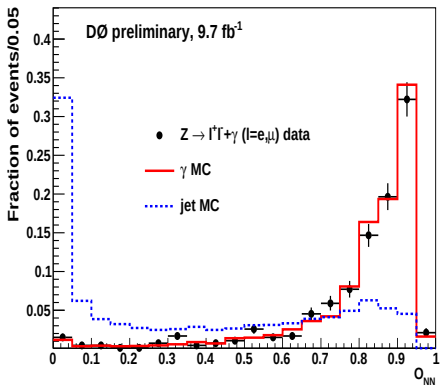

FIG. 1: Normalized distributions of O_{NN} from real and fake photons.

IV. BACKGROUNDS

There are three major sources of background to the $H \to \gamma\gamma$ signature: (i) Drell-Yan events where both electrons are misidentified as photons; (ii) γ+jet and jet+jet events where the jet(s) is (are) misidentified as photon(s); (iii) direct di-photon events. The modeling of the individual backgrounds is described in the following sections.

A. Drell-Yan $Z/\gamma^* \to ee(\tau\tau)$ contribution

We use $Z/\gamma^* \to ee(\tau\tau)$ ALPGEN [24]+ PYTHIA MC samples to estimate the Drell-Yan contribution. The NNLO cross section [25] is used for the normalization. From the $Z/\gamma^* \to ee$ MC samples, we find that 2% of the electrons can pass the photon selection requirements described in Section III due to tracker inefficiencies. The total background contribution from the Drell-Yan process is found to be 858 ± 14 events.

B. γ+jet and di-jet background

We estimate the γ + jet and di-jet contributions from the data after the event selection is applied (see section III) by using the method described in detail in Ref. [26]. This method is implemented on a event-by-event basis. In this analysis, we use $O_{NN} = 0.75$ as a boundary to classify the candidates into four categories, defined below. We have determined that choice of $O_{NN} = 0.75$ minimizes the statistical uncertainties of the classification.

- N_{pp} have both photon candidates with $O_{NN} > 0.75$;
- N_{pf} have the leading (highest p_T) photon candidate with $O_{NN} > 0.75$, but the sub-leading $O_{NN} < 0.75$;
- N_{fp} have the leading photon candidate with $O_{NN} < 0.75$, but the sub-leading $O_{NN} > 0.75$;
- N_{ff} have both photon candidates with $O_{NN} < 0.75$.

The Drell-Yan Z/$\gamma^* \to ee(\tau\tau)$ contributions to (N_{pp}, N_{pf}, N_{fp}, N_{ff}) are determined from a Monte Carlo simulation and are subtracted. The pass-fail vector (N_{pp}, N_{pf}, N_{fp}, N_{ff}) thus obtained is related to the $(N_{\gamma\gamma}, N_{\gamma j}, N_{j\gamma}, N_{jj})$ vector as follows:

$$\begin{pmatrix} N_{ff} \\ N_{fp} \\ N_{pf} \\ N_{pp} \end{pmatrix} = E \times \begin{pmatrix} N_{jj} \\ N_{j\gamma} \\ N_{\gamma j} \\ N_{\gamma\gamma} \end{pmatrix} \tag{1}$$

where $N_{\gamma\gamma}$ is the number of γ+γ events, $N_{\gamma j}$ and $N_{j\gamma}$ are the number of γ+jet events and N_{jj} is the number of di-jet events. The 4×4 matrix E is defined as:

$$\begin{pmatrix} (1-\epsilon_{j1})(1-\epsilon_{j2}) & (1-\epsilon_{j1})(1-\epsilon_{\gamma 2}) & (1-\epsilon_{\gamma 1})(1-\epsilon_{j2}) & (1-\epsilon_{\gamma 1})(1-\epsilon_{\gamma 2}) \\ (1-\epsilon_{j1})\epsilon_{j2} & (1-\epsilon_{j1})\epsilon_{\gamma 2} & (1-\epsilon_{\gamma 1})\epsilon_{j2} & (1-\epsilon_{\gamma 1})\epsilon_{\gamma 2} \\ \epsilon_{j1}(1-\epsilon_{j2}) & \epsilon_{j1}(1-\epsilon_{\gamma 2}) & \epsilon_{\gamma 1}(1-\epsilon_{j2}) & \epsilon_{\gamma 1}(1-\epsilon_{\gamma 2}) \\ \epsilon_{j1}\epsilon_{j2} & \epsilon_{j1}\epsilon_{\gamma 2} & \epsilon_{\gamma 1}\epsilon_{j2} & \epsilon_{\gamma 1}\epsilon_{\gamma 2} \end{pmatrix} \tag{2}$$

where $\epsilon_{\gamma 1}$ and $\epsilon_{\gamma 2}$ are the fractions of the leading and sub-leading photons that have passed the event selection and have $O_{NN} > 0.75$, and ϵ_{j1} and ϵ_{j2} are the fractions of jets that have passed the event selection and have $O_{NN} > 0.75$. The photon efficiency (ϵ_γ) [27] is estimated using direct di-photon MC and corrected for small differences between data and the simulation measured in pure samples of photon events from radiative Z decays $Z \to \ell^+\ell^-\gamma$ ($\ell = e, \mu$). The jet efficiency (ϵ_j) [27] is estimated using di-jet MC enriched in jets misidentified as photons and cross-checked in jet samples in data. Both efficiencies are parameterized as a function of photon pseudorapidity. $(N_{\gamma\gamma}, N_{\gamma j}, N_{j\gamma}, N_{jj})$ are obtained by solving equation (1). Table I shows the results after applying this method to the data.

(a)

N_{ff}	2719
N_{fp}	3600
N_{pf}	4916
N_{pp}	7796
Data	19031

(b)

N_{DY}	795 ± 17
N_{jj}	3330 ± 222
$N_{\gamma j} + N_{j\gamma}$	5738 ± 406
$N_{\gamma\gamma}$	9168 ± 262
Data	19031

TABLE I: (a) shows the number of events in the data for the 4 categories. (b) shows the number of $\gamma\gamma$, γ+jet and di-jet events in the data from the 4x4 matrix method. The number of DY events is estimated from MC. The quoted uncertainties are statistical only.

Due to the limited statistics of non-$\gamma\gamma$ (sum of γ+jet and di-jet) events, especially in the high mass region, we reverse the initial event selection cut (*ie* $O_{NN} < 0.1$) on one or both of the two photon candidates to obtain an enriched γ+jet or di-jet orthogonal sample from data. We find that the kinematic distributions of the orthogonal sample are in good agreement with the non-$\gamma\gamma$ events from the 4×4 matrix method. Therefore we model the non-$\gamma\gamma$ background using the orthogonal sample normalized by the corresponding numbers of non-$\gamma\gamma$ events from the 4x4 matrix method.

C. Direct di-photon production

We use the SHERPA [28] Monte Carlo generator to model the direct $\gamma\gamma$ background shape and use the di-photon component of the 4x4 matrix method for the normalization. The inclusive cross section of SHERPA has leading order accuracy while the photon fragmentation function is modeled by an interleaved QCD+QED parton shower including higher-order real-emission matrix elements.

V. FINAL DISCRIMINANT DISTRIBUTIONS

In order to improve the overall sensitivity of this analysis, we use the gradient Boosted Decision Tree method from the Toolkit for Multivariate Analysis [13] that combines ten kinematic variables to build a final discriminant between the signal and background. The ten kinematic variables are,

- leading photon transverse momentum, p_T^1
- sub-leading photon transverse momentum, p_T^2
- di-photon invariant mass, $M_{\gamma\gamma}$
- di-photon transverse momentum, $p_T^{\gamma\gamma}$
- azimuthal angle between the two photon candidates, $\Delta\phi_{\gamma\gamma}$
- cosθ^*, in the Collins-Soper frame [29]
- ϕ^*, in the Collins-Soper frame
- leading photon ANN output, O_{NN}^1
- sub-leading photon ANN output, O_{NN}^2
- missing transverse energy $\not{E}_T$

Amongst these ten variables, while $M_{\gamma\gamma}$ provides the most power to distinguish signal from backgound, kinematic variables such as p_T^1, p_T^2, $p_T^{\gamma\gamma}$, $\Delta\phi_{\gamma\gamma}$, cos$\theta^*$ and ϕ^* are used to separate signal from the non-resonant backgound in momentum and angular distributions. Moreover, photon identification variables such as O_{NN}^1 and O_{NN}^2 are included to further reject the residual background from misidentified photons.

Figures 2 and 3 show these ten kinematic distributions from data, backgrounds and the $M_H = 125$ GeV signal. The background modeling agrees well with data. Figure 4 shows an enlarged view of the mass spectrum. Only the signal and background samples with a di-photon invariant mass within 30 GeV of the assumed value of M_H mass are used in training the MVA used to discriminate the Higgs boson signal for each mass point.

To minimize the impact from systematic uncertainties, we separate the MVA output into two categories: the photon dominated region (both photon candidates with $O_{NN} > 0.75$) and the jet dominated region (at least one photon candidate $O_{NN} < 0.75$). To further constrain background normalizations, we also use the invariant mass spectrum outside the mass window (sideband) as the final discriminant. Therefore for each mass point, there are four "channels": two MVA outputs in the photon/jet dominated regions and two corresponding sidebands.

As an illustration, we show the four final discriminants for M_H=125 GeV in Fig. 5(linear) and Fig. 6(log).

Table II shows the signal, backgrounds (after having fitted the nuisance parameters, *cf.* Section VII) and data yields for six of the assumed Higgs masses within the ±30 GeV mass window.

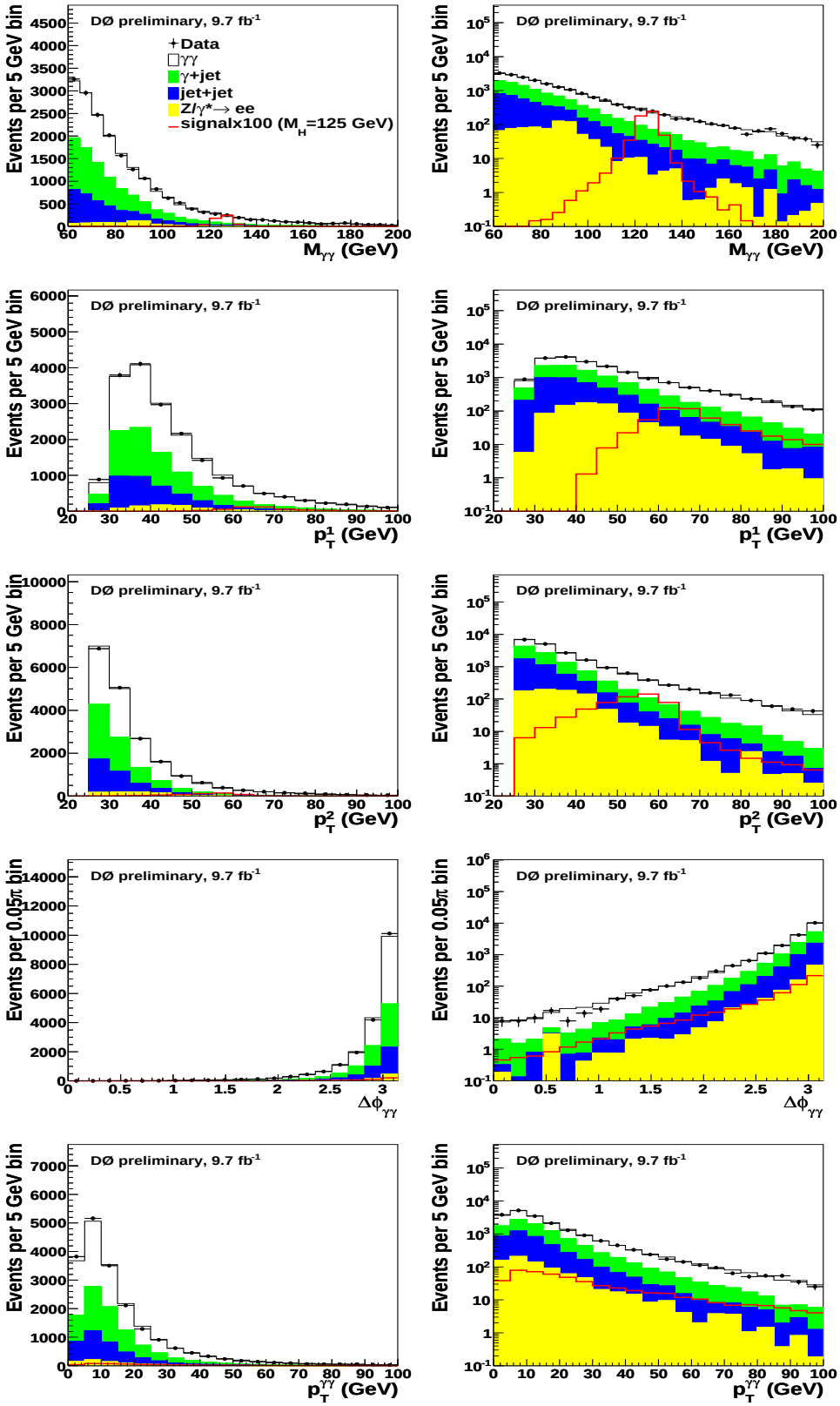

FIG. 2: Data and background modeling comparisons in terms of p_T^1, p_T^2, $M_{\gamma\gamma}$, $\Delta\phi^{\gamma\gamma}$ and $p_T^{\gamma\gamma}$ for the mass region [60, 200] GeV. A signal for $M_H = 125$ GeV, multiplied by 100 is also shown. The plots in the left column are on a linear scale and the plots in the right column are on a log scale. The legend is shown in top left plot.

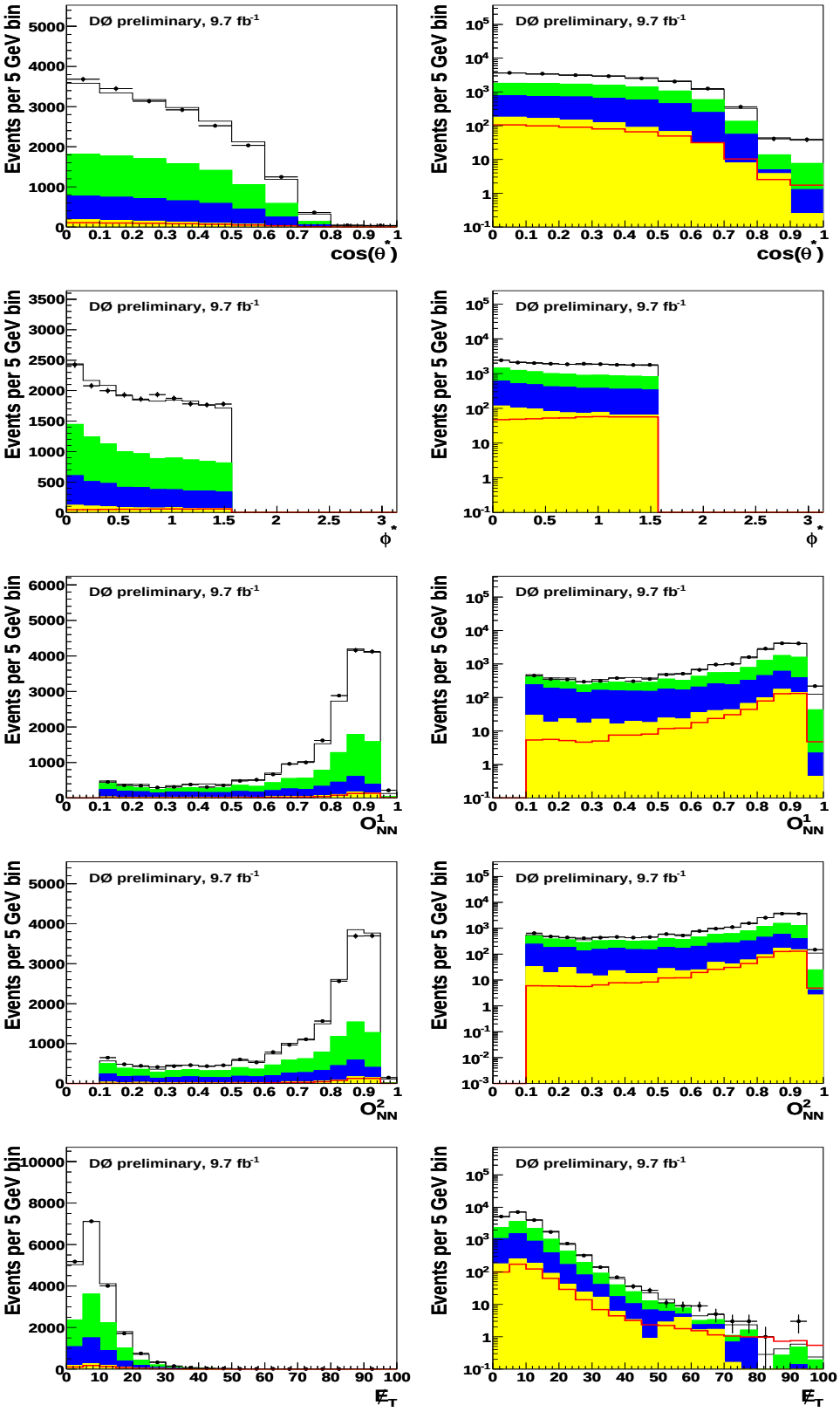

FIG. 3: Data and background modeling comparisons in terms of cosθ^*, ϕ^*, ONN^1, ONN^2 and $\not\!\!E_T$ for the mass region [60, 200] GeV. A signal for $M_H = 125$ GeV, multiplied by 100 is also shown. The plots in the left column are on a linear scale and the plots in the right column are on a log scale. The legend is the same as Fig. 2.

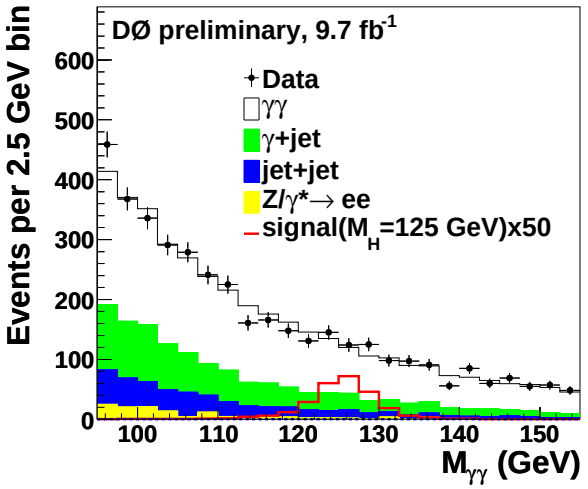

FIG. 4: Data and background modeling comparison in $M_{\gamma\gamma}$. A signal for $M_H = 125$ GeV, multiplied by 100 is also shown.

TABLE II: SM signal, backgrounds and data yields from 100 GeV to 150 GeV in 10 GeV intervals within the [M_H - 30 GeV, M_H + 30 GeV] mass window. The quoted uncertainties are statistical and systematic.

M_H (GeV)	100	110	120	130	140	150
$\gamma\gamma$ (DDP)	5843 ± 33 ± 133	4031 ± 27 ± 89	2848 ± 22 ± 64	2061 ± 19 ± 45	1508 ± 13 ± 32	1120 ±10 ± 25
$\gamma + jet$	3386 ± 33 ± 175	2035 ± 25 ± 95	1194 ± 19 ± 57	716 ± 15 ± 34	441 ± 12 ± 21	286 ± 9 ± 14
$jet + jet$	1926 ± 26 ± 141	1016 ± 19 ± 80	573 ± 14 ± 45	334 ± 11 ± 26	200 ± 8 ± 15	128 ±7 ± 10
$Z/\gamma^* \to e^+e^-$	473 ± 29 ± 80	407 ± 23 ± 59	241 ± 18 ± 34	83 ± 10 ± 12	37 ± 6 ± 5	24 ±6 ± 3
Total background	11628 ± 61 ± 128	7489 ± 47 ± 82	4856 ± 37 ± 58	3194 ± 28 ± 38	2186 ± 20 ± 28	1558 ± 16 ± 22
Data	11578	7434	4873	3182	2166	1606
H signal	6.44 ± 0.09± 0.64	6.33 ± 0.09± 0.63	5.72 ± 0.08± 0.57	4.65 ± 0.09± 0.45	3.23 ± 0.08± 0.31	1.90± 0.02± 0.19

VI. SYSTEMATIC UNCERTAINTIES

The MVA output is used as the discriminating variable in the search for the $H \to \gamma\gamma$ decay. We estimate systematic uncertainties for both signal and backgrounds that affect the normalization and shape of the MVA output as described below.

- 6.1% uncertainty on the integrated luminosity [30] affecting signal and Drell-Yan background normalization;
- theoretical cross section uncertainties (including scale and PDF uncertainties) for signal (GF (14.1%), VH (6.2%) and VBF (4.9%));
- 3% uncertainty on the photon identification efficiency affecting signal and Drell-Yan background normalization;
- 0.7-1.0% uncertainty on the signal acceptance from the PDFs uncertainty, estimated using the CTEQ6M [31] error functions;
- 1-5% uncertainty on the signal shape from gluon fusion p_T reweighting to the spectrum from the HqT [32] NNLO event generator;
- 9% uncertainty on the track veto efficiency and 4% on the cross section affecting the Drell-Yan background normalization;
- 1.5% uncertainty on the photon $O_{NN} > 0.75$ efficiency in the 4×4 matrix method affecting the normalization and shape of the non-$\gamma\gamma$ and $\gamma\gamma$ backgrounds;
- 10% uncertainty on the jet $O_{NN} > 0.75$ efficiency in the 4×4 matrix method affecting the normalization and shape of the non-$\gamma\gamma$ and $\gamma\gamma$ backgrounds;

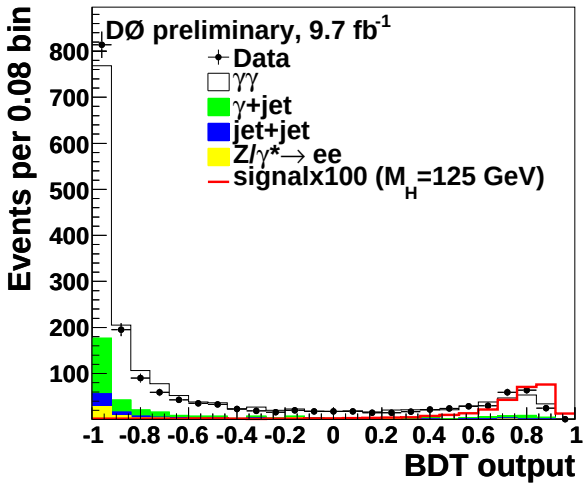

(a)photon dominated region

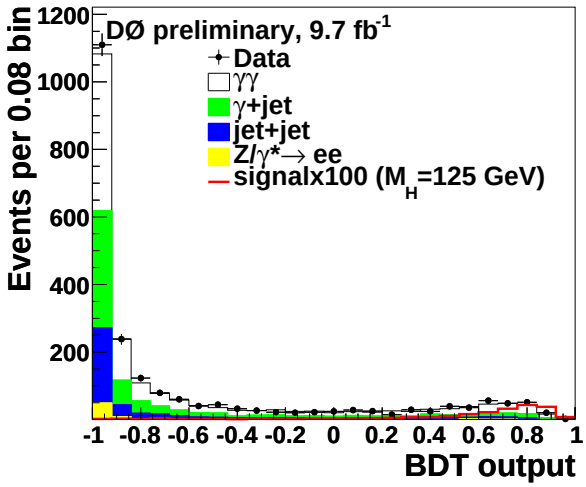

(b)jet dominated region

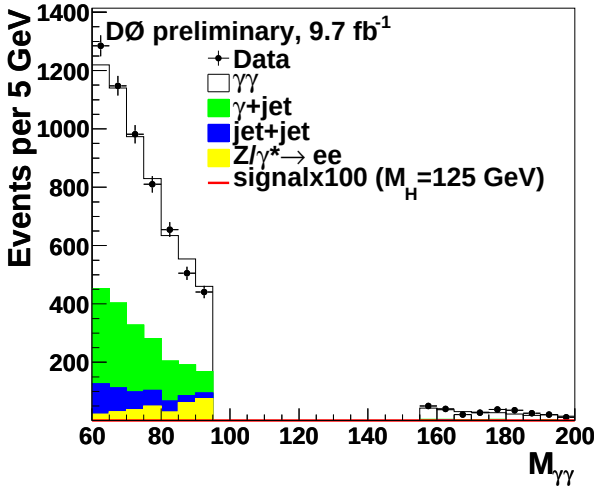

(c)photon dominated region sideband

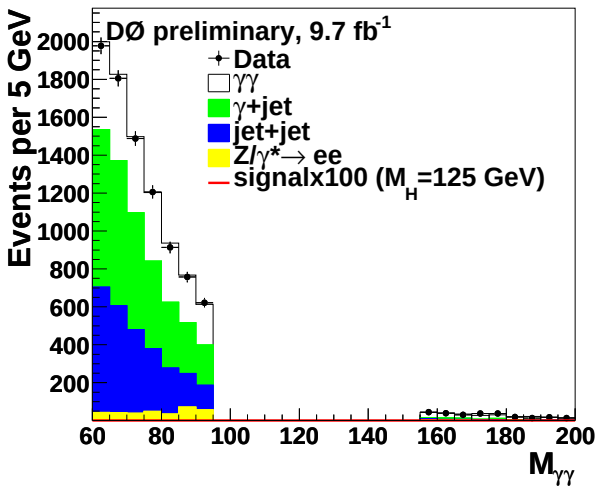

(d)jet dominated region sideband

FIG. 5: final discriminants for 125 GeV signal in linear scale.

- 10-20% uncertainty on the shape of the MVA output from the factorization and renomalization scale of SHERPA affecting the $\gamma\gamma$ background shape.

VII. RESULTS

Since we do not observe evidence for a SM Higgs signal, we set upper limits on the Higgs production cross section times branching ratio for a Higgs decaying into a pair of photons, using the final discriminant distributions detailed in Section V for each mass point. Limits are calculated at the 95% C.L. using the modified frequentist CL_s approach with a Poisson log-likelihood ratio test statistic [33, 34]. We treat systematic uncertainties as nuisance parameters constrained by their priors, and the best fits of these parameters to data are determined at each value of M_H by maximizing the likelihood ratio [34]. The fitted values of the nuisance parameters from B-only and S+B hypothesis are within 1σ of their priors.

As an illustration, the distribution of the BDT output for data, after background subtraction, is shown in Fig. 7.

The log-likelihood ratio and 95% C.L. upper limits on the cross section times branching ratio relative to the SM prediction are displayed in Fig. 8 as a function of Higgs boson mass. The values of the limits are also given in Table III. Variations in the log-likelihood ratio and 95% C.L. upper limits as a function of Higgs boson mass are consistent

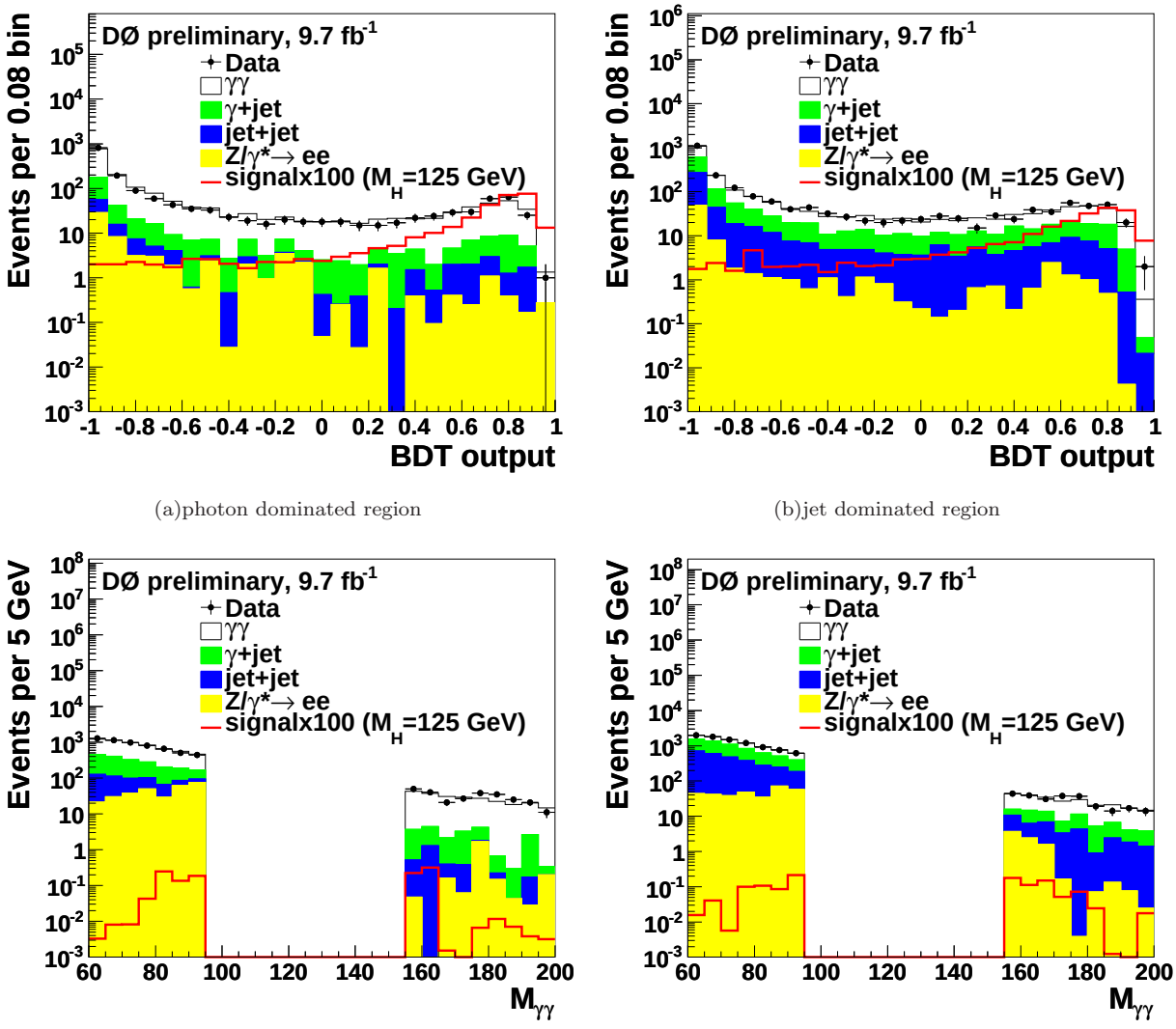

(a)photon dominated region

(b)jet dominated region

(c)photon dominated region sideband

(d)jet dominated region sideband

FIG. 6: final discriminants for 125 GeV signal in log scale.

Higgs mass(GeV)	100	105	110	115	120	125	130	135	140	145	150
observed limit	11.9	17.0	10.7	6.3	10.8	12.6	13.3	10.4	12.8	16.4	22.0
expected limit	11.8	10.3	9.6	9.3	9.3	8.2	8.5	10.0	10.5	13.1	16.6
SM $\sigma \times BR$(fb)	3.5	3.4	3.3	3.2	3.0	2.7	2.4	2.1	1.7	1.3	1.0

TABLE III: 95% C.L. observed and expected limits on $\sigma \times BR$ relative to the SM prediction for different Higgs masses. Also shown are the SM predictions of $\sigma \times BR$.

with statistical fluctuations in the background prediction given the ∼3 GeV mass resolution of this search.

VIII. SUMMARY

We have presented a search for the SM Higgs boson in the di-photon channel using 9.7 fb^{-1} of D0 Run II data. Good agreement between the data and the SM background prediction is observed. Since there is no evidence for new physics, we set 95% C.L. limits on the production cross section times the branching ratio ($\sigma \times BR(H \to \gamma\gamma)$) relative to the SM Higgs prediction for different assumed Higgs masses. The expected limits are below 10 between 110 and 130 GeV, with a minimum of 8.2 at 125 GeV. The observed limits at 110, 125 and 135 GeV are 8.0, 12.9 and 13.7. By

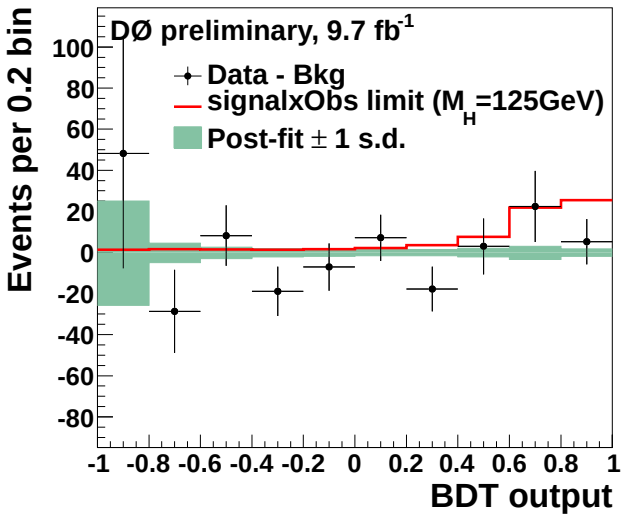

FIG. 7: Post-fit background subtracted data distribution for $M_H = 125$ GeV. The signal is scaled by the observed limit. The green area shows the post-fit 1 standard deviation (s.d.) under the B only hypothesis.

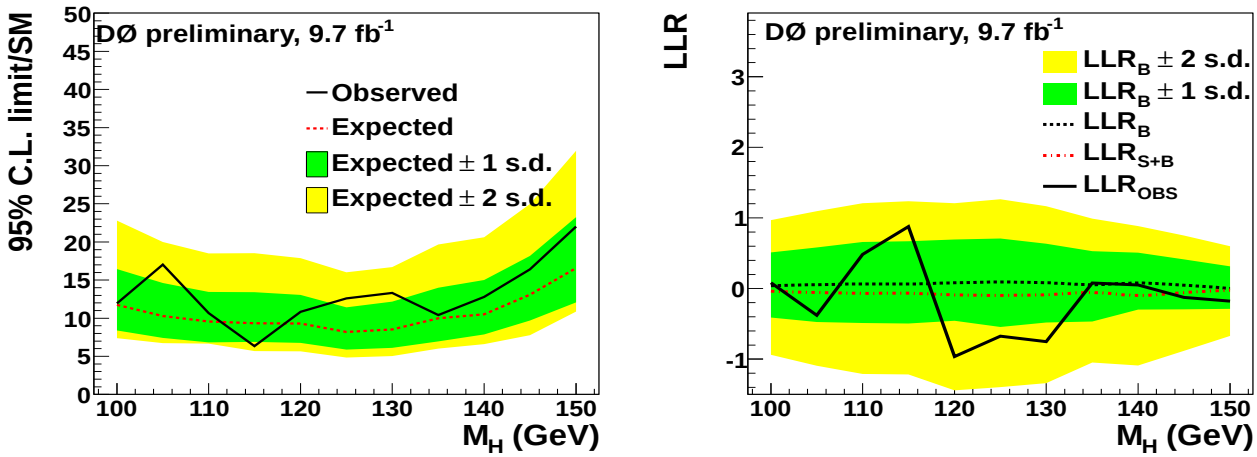

(a) (b)

FIG. 8: (a) Observed and expected 95% C.L. limits on the $\sigma \times BR$ relative to the SM prediction as a function of Higgs mass. The green and yellow bands correspond to 1 and 2 standard deviations (s.d.) around the expected limit. (b) Observed log-likelihood ratio (LLR) as a function of M_H compared to the expected LLR for the background-only hypothesis and signal+background hypothesis. The green and yellow bands correspond to the 1 s.d. and 2 s.d. around the expected LLR.

comparison with our previous result using 9.7 fb^{-1} [12], the expected limits in this analysis are improved by $\sim 28\%$ mainly due to the categrorization detailed in Section V.

Acknowledgments

We thank the staff at Fermilab and collaborating institutions, and acknowledge support from the DOE and NSF (USA); CEA and CNRS/IN2P3 (France); FASI, Rosatom and RFBR (Russia); CAPES, CNPq, FAPERJ, FAPESP and FUNDUNESP (Brazil); DAE and DST (India); Colciencias (Colombia); CONACyT (Mexico); KRF and KOSEF (Korea); CONICET and UBACyT (Argentina); FOM (The Netherlands); STFC (United Kingdom); MSMT and GACR (Czech Republic); CRC Program, CFI, NSERC and WestGrid Project (Canada); BMBF and DFG (Germany); SFI (Ireland); The Swedish Research Council (Sweden); CAS and CNSF (China); and the Alexander von Humboldt

Foundation.

---

[1] ALEPH, DELPHI, L3, and OPAL Collaborations, The LEP Working Group for Higgs Boson Searches, Phys. Lett. B **565**, 61 (2003).
[2] The LEP Electroweak Working Group, "Status of March 2012" http://lepewwg.web.cern.ch/LEPEWWG/
[3] T. Aaltonen *et al.* (CDF Collaboration), Phys. Rev. Lett. **108**, 151803 (2012).
[4] V.M. Abazov *et al.* (D0 Collaboration), Phys. Rev. Lett. **108**, 151804 (2012). T. Aaltonen *et al.* (CDF and D0 Collaborations), FERMILAB-CONF-10-257-E, arXiv:1007.4587, (2010).
[5] S. Chatrchyan *et al.* (CMS Collaboration), Phys. Lett. B **710** 26-48, (2012).
[6] G. Aad *et al.* (ATLAS Collaboration), Phys. Lett. B **710** 49-66, (2012).
[7] S. Chatrchyan *et al.* (CMS Collaboration), Phys. Lett. B **710** 403-425 (2012).
[8] G. Aad *et al.* (ATLAS Collaboration), Phys. Rev. Lett. **108**, 111803 (2012).
[9] CMS Collaboration, arXiv:1202.1997, (2012).
[10] G. Aad *et al.* (ATLAS Collaboration), Phys. Lett. B. **710**, 383-402 (2012).
[11] S. Mrenna and J. Wells, Phys. Rev. D **63**, 015006 (2000).
[12] D0 Collaboration, "Search for the Standard Model Higgs Boson in $\gamma\gamma + X$ final states at D0 using 9.7 fb^{-1} data", D0 Note **6295-CONF** (2012).
[13] A. Hoecker *et al.*, TMVA 4 Toolkit for Multivariate Data Analysis with ROOT Users Guide, arXiv:physics/0703039 (2007).
[14] V. M. Abazov *et al.*, Nucl. Instrum. Meth. A **565**, 463 (2006). M. Abolins *et al.*, Nucl. Instrum. Methods Phys. Res. A **584**, 75 (2008); R. Angstadt *et al.*, Nucl. Instrum. Methods Phys. Res. A **622**, 298 (2010).
[15] The polar angle θ and the azimuthal angle ϕ are defined with respect to the positive z axis, which is along the proton beam direction. Pseudorapidity is defined as $\eta = ln[tan(\theta/2)]$. η_{det} and ϕ_{det} are the pseudorapidity and the azimuthal angle measured with respect to the center of the detector.
[16] T. Sjöstrand *et al.*, Comput. Phys. Commun. **135**, 238 (2001). We use PYTHIA version v6.323 with Tune A.
[17] H.L. Lai *et al.*, Phys. Rev. D **55**, 1280 (1997).
[18] R. Brun and F. Carminati, CERN Program Library Long Writeup W5013, 1993 (unpublished).
[19] C. Anastasiou, R. Boughezal, and F. Petriello, J. High Energy Phys. **04**, 003 (2009);
D. Florian and M. Grazzini, Phys. Lett. B **674**, 291 (2009).
J. Baglio and A. Djouadi, J. High Energy Phys. **10**, 064 (2010).
P. Bolzoni, F. Maltoni, S.-O. Moch, and M. Zaro, Phys. Rev. Lett. **105**, 011801 (2010).
The Tevatron New Phenomena and Higgs Working Group, "Cross Section and Branching Ratio Recommendations for Tevatron Higgs Searches", (2012).
[20] A. Djouadi, J. Kalinowski and M. Spira, Comput. Phys. Commun. **108**, 56 (1998).
[21] U. Aglietti *et al.*, arXiv:hep-ph/0610033 (2006).
[22] C. Peterson, T. Rognvaldsson and L. Lonnblad, "JETNET 3.0 A versatile Artificial Neural Nertwork Package", Lund University Preprint LU-TP 93-29. Version 3.5 is used here.
[23] D0 Collaboration, "Search for the standard model Higgs boson in di-photon final states at DZero with 4.2 fb^{-1} data", D0 Note **5858-CONF** (2009).
[24] M.L. Mangano, M. Moretti, F. Piccinini, R. Pittau, A. Polosa, JHEP 0307:001 (2003).
[25] R. Hamberg, W. L. van Neerven and T. Matsuura, Nucl. Phys. B **359**, 343 (1991) [Erratum-ibid. B **644**, 403 (2002)].
[26] Y. Liu, Ph.D. thesis, Fermilab [FERMILAB-THESIS-2004-37] (2004).
[27] V. M. Abazov *et al*, (D0 Collaboration), Phys. Rev. Lett. **107**, 151801 (2011).
[28] T. Gleisberg *et al.* J. High Energy Phys. **02**, 007 (2009).
[29] J.C. Collins and D.E. Soper, Phys. Rev. D **16**, 2219 (1977).
[30] T. Andeen *et al.*, FERMILAB-TM-2365 (2007).
[31] J. Pumplin *et al.*, JHEP **0207**, 012 (2002).
[32] G. Bozzi, S. Catani, D. de Florian, and M. Grazzini, Phys. Lett. B **564** 65 (2003);
Nucl. Phys. **B737**, 73 (2006).
[33] T. Junk, Nucl. Intrum. Meth. A **434**, 435 (1999); A. Read, CERN 2000-005 (30 May 2000).
[34] W. Fisher, FERMILAB-TM-2386-E (2006).